Fluid Phase Equilibria 360 (2013) 456–465

Contents lists available at ScienceDirect

Fluid Phase Equilibria

journal homepage: www.elsevier.com/locate/fluid

Methane and carbon dioxide adsorption in clay-like slit pores by Monte Carlo simulations

Zhehui Jin [a], Abbas Firoozabadi [a,b,*]

[a] Reservoir Engineering Research Institute, United States
[b] Yale University, United States

ARTICLE INFO

Article history:
Received 28 June 2013
Received in revised form
17 September 2013
Accepted 21 September 2013
Available online 29 September 2013

Keywords:
Shale
Clay

ABSTRACT

Shale is composed of two distinct permeable media: (1) inorganic, and (2) organic. Both media may contribute to the amount of hydrocarbon and non-hydrocarbon species in shale. In this work, we investigate sorption in clay minerals which may constitute most of the inorganic matter in shale. We represent the inorganic matter by the montmorillonite clays with different charges for different atoms. Sorption of methane and carbon dioxide is investigated by Monte Carlo simulations. In this work, we assume that methane is structureless and CO_2 is assumed to have structure and we assign partial charges to its atoms. Our results indicate that charge affects the orientation of CO_2 molecules close to the surface and plays an important role in CO_2 sorption. Methane sorption is found to be mainly a function of surface area. We also incorporate cation exchange in clay description and model its effect on sorption. Cation exchange increases CO_2 sorption at low pressure significantly and as pressure increases, the effect becomes less pronounced. Cation exchange also affects orientation of CO_2 molecules near the surface. Results from our simulation are expected to provide insight into phase behavior in clays, a major constituent of shale media.

© 2013 Elsevier B.V. All rights reserved.

1. Introduction

Shale gas is an important unconventional energy resource; it has had a game changing effect on natural gas supply in the US in recent years. Despite the huge impact, we know very little on some fundamental aspects related to the phase behavior and local species distribution in shale permeable media. The fluid samples from shale light oil formations may be highly undersaturated. However, when production starts, the ratio of gas to liquid may increase significantly. Such a phase behavior is drastically different from that in conventional formations. The modeling of phase behavior in shale gas and shale light oil formations provides knowledge related to well production rate. In the literature, there is neither a molecular model nor a macroscopic-based model that can describe phase behavior in shale formation.

One of the challenges in the shale gas and shale light oil formations is well productivity and gas-in-place (GIP) estimation [1]. The contribution of the adsorbed gas to the total GIP can be as much as 60% [2]. However, there is currently no sound theory to predict the sorbed gas in shale media mainly due to complex nature of shale media. Shale is comprised of two distinct parts: inorganic and organic materials. The organic material is mainly composed of kerogen, which is a mixture of organic chemical compounds. A study [3] suggests that gas sorption and gas solubility in organic materials may provide bulk of the gas-in-place in shale gas reservoirs. The common belief is that the amount of adsorbed gas is proportional to the content of organic matter. A number of papers present data relating a correlation between methane sorption to the total organic content of organic-rich shales [3–5].

A few studies have shown that the clay mineral composition and its micropore structure also affect gas sorption of organic-rich shales [6–8]. There are indications that clay minerals affect sorption in clay-rich shales [9–11]; sorption in clay-rich shales can be comparable to that of total-organic-carbon (TOC) shales. Clay minerals have micropore-to-mesopore structures which provide surface area for gas adsorption depending on the pore structures and clay chemical compositions. The surface area of shale rocks is in the range of 5–50 m^2/g [3]. The surface area of clay minerals is reported to be in the range of 10–25 m^2/g [12]. The surface areas in shale and clay minerals are, therefore, comparable. The clay-rich shales provide a significant portion of mesoporosity [3]; we may not therefore predict the GIP in shales only based on the TOC contents. Experimental work [13] has shown that pores of 1–2 nm width in the interlayers of clay minerals provide the adsorption sites for gases due to large surface area. In this microscopic scale, the properties of species are greatly different from that in bulk. Unlike simple carbonaceous porous media, clay minerals exhibit morphological

* Corresponding author at: Reservoir Engineering Research Institute, United States. Tel.: +1 650 326 9259.
E-mail address: af@rerinst.org (A. Firoozabadi).

0378-3812/$ – see front matter © 2013 Elsevier B.V. All rights reserved.
http://dx.doi.org/10.1016/j.fluid.2013.09.047

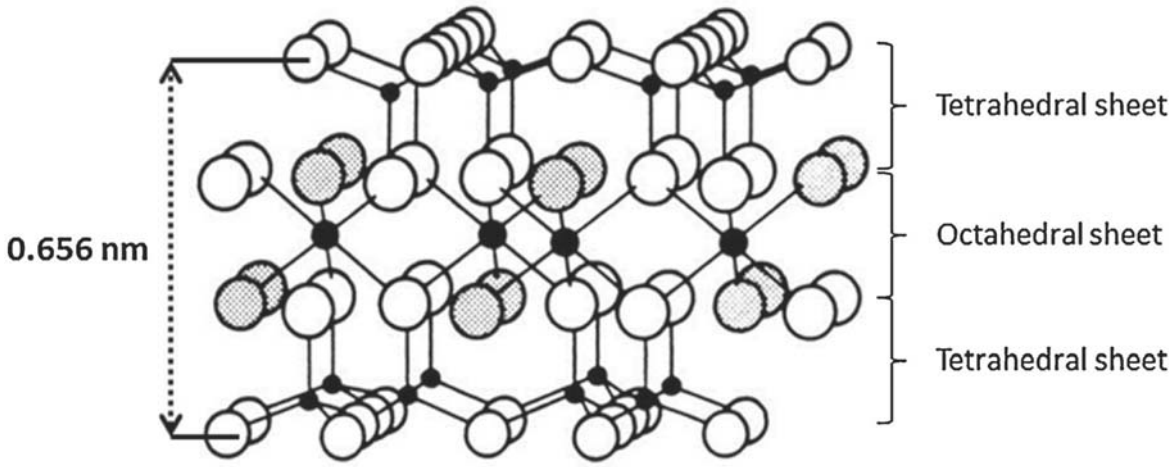

Fig. 1. The schematic representation of 2:1 layer type clay minerals obtained from Ref. [31]. The open spheres represent O, the shaded spheres represent OH, the small solid spheres depict Si and the large solid spheres are Al.

disorder and heterogeneous chemistry. Such chemical heterogeneity will likely affect gas sorption and sorbed gas phase equilibrium [14]. Currently the underlying mechanisms of gas sorption in clay minerals are not well understood.

Extensive molecular simulation studies [15–18] are reported on water adsorption and swelling in clay minerals. However, gas sorption in clay minerals has been rarely studied. Most of molecular simulations of gas sorption are focused on the activated-carbon slit pores [19–23], where chemical heterogeneity may not be relevant. The chemical heterogeneity of the pores may have significant effect on gas sorption under confinement [14,24–26]. Unlike the conventional carbonaceous materials, due to mineralogy [27], gas sorption in clay minerals not only depends on pore structure but also on the chemical heterogeneity. Experimental research has demonstrated the efficacy of intercalating gas molecules in clays [28]. There are only a handful of molecular simulations on gas sorption in clay minerals. Cygan et al. [29] used *NpT* and *NVT* molecular dynamics (MD) to investigate carbon dioxide intercalation mechanism in the interlayer of montmorillonite clays and the effect of molecular flexibility on diffusion rate of CO_2 in water by a flexible force field. Yang and Zhang [19] used MD in an *NVT* ensemble to study the structure and diffusion of dense CO_2 in clay-like slit pores. The effect of pore structure and chemical heterogeneity on gas sorption and structure in clay minerals has yet to be investigated. A drawback of *NpT* or *NVT* ensemble simulations is that they cannot provide gas content in clays. In this work, we use the grand canonical Monte Carlo (GCMC) simulations to investigate the effect of clay pore structure and chemical heterogeneity on methane and CO_2 sorption in clay-like slit pores. Methane is the main constituent of natural gases. Carbon dioxide can be potentially sequestered in shale formations. It is also found in the subsurface together with methane.

Clays are generally made of large particles formed by stacks of sheets [30]. Similar to gas sorption modeling in carbonaceous materials, we assume that the inter-pore interactions are negligible and gas adsorbs in nanometer slit-like pores. The solid surface in our work has a structure and charge of the montmorillonite clay which has two tetrahedral sheets fused to an octahedral sheet [31] as shown in Fig. 1. Two of the octahedral positions of the montmorillonite clay are filled by the trivalent Al atoms; such an electroneutral 2:1 clay mineral is called pyrophyllite [32]. Montmorillonite clays consist of negatively charged silicate layers with Si atoms replaced by Al atoms in the tetrahedral sheet and Al atoms replaced by Mg atoms in the octahedral sheet [32]. The negative charges are compensated by interlayer counterions [15,32]. The focus of this work is on gas sorption in a neutral slit-like aluminum-silicate mineral and slit-like montmorillonite clay mineral with cation exchange. We use a full atomistic pore structure of clay by duplicating the unit cell of montmorillonite clay proposed by Skipper et al. [33]. This unit cell has been widely used in molecular simulations of water and hydrate formation in clay minerals [15,32,34–36]. Methane molecule is simulated by single-site Lennard–Jones particles and CO_2 molecule is modeled by three-site particles explicitly considering the short-range van der Waals and long-range electrostatic interactions. By incorporating these features, our GCMC is expected to provide the effect of both pore structure and chemical heterogeneity on gas sorption in clay-like slit pores.

The remainder of this paper is organized as follows. In Section 2, we introduce the molecular simulation methods and define the molecular models. In Section 3, we investigate methane and CO_2 sorption in clay-like slit pores with various pore sizes and bulk pressures of the gas molecules. In Section 4, we summarize the key conclusions and discuss implications.

2. Simulation method

2.1. Model

We use a fixed solid surface of montmorillonite clay as a 2:1 clay mineral. The neutral montmorillonite has the unit-cell formula $Si_8Al_4O_{20}(OH)_4$ [15]. The simulation cell contains two 32-clay unit cells resulting in a clay patch of 4.224 nm × 3.656 nm with a thickness of 0.656 nm separated by a fixed distance to represent a clay nanopore. In molecular dynamics simulations [19], two half-layers of the solid sheets have been used to investigate the structure of dense carbon dioxide in a clay-like slit pore. But in a simulation study of water adsorption in montmorillonite clays, it has been shown that the two-clay-sheets provide more accurate results than the one-clay-sheet, especially at small basal spacings [32]. The positions and charges of the sites in the unit cell of the clay are shown in Table 1 [33]. The positions and charges from Ref. [33] are widely used in simulations of water adsorption in clay and validated by comparing simulations to experimental data [32,35,36]. The unit cell that constitutes the clay sheet in our work is shown in Table 1.

For montmorillonite clay with cation exchange, the unit cell formula is $Na_{0.75}(Si_{7.75}Al_{0.25})(Al_{3.5}Mg_{0.5})O_{20}(OH)_4$ [32]. Based on this formula, each of our clay sheets with 32 unit cells have 16 isomorphous trivalent Al atoms replaced by divalent Mg atoms in the octahedral sheet, 8 isomorphous replacements of tetravalent Si atoms by trivalent Al atoms in the tetrahedral sheet, and 24

Table 1
Atomic positions and effective charges in the unit cell [33] and charges in CO_2 [40].

Atom	x (nm)	y (nm)	z (nm)	q (e)
O	0.264	0.0	0.328	−0.8
O	0.132	0.228	0.328	−0.8
O	0.396	0.228	0.328	−0.8
O(OH)	0.0	0.0	0.106	−1.7175
H(OH)	0.08815	0.0	0.1434	0.7175
Si	0.264	0.152	0.273	1.2
Si	0.0	0.305	0.273	1.2
O	0.264	0.152	0.106	−1.0
O	0.0	0.305	0.106	−1.0
Al	0.44	0.152	0.0	3.0
Al	0.44	−0.152	0.0	3.0
O	0.0	0.457	0.328	−0.8
O	0.396	0.685	0.328	−0.8
O	0.132	0.685	0.328	−0.8
O(OH)	0.264	0.457	0.106	−1.7175
H(OH)	0.35215	0.457	0.1434	0.7175
Si	0.0	0.609	0.273	1.2
Si	0.264	0.762	0.273	1.2
O	0.0	0.609	0.106	−1.0
O	0.264	0.762	0.106	−1.0
Al	0.704	0.609	0.0	3.0
Al	0.704	0.305	0.0	3.0
O	0.088	0.914	−0.328	−0.8
O	0.22	0.686	−0.328	−0.8
O	−0.044	0.686	−0.328	−0.8
O(OH)	0.352	0.914	−0.106	−1.7175
H(OH)	0.26385	0.914	−0.1434	0.7175
Si	0.088	0.762	−0.273	1.2
Si	0.352	0.609	−0.273	1.2
O	0.088	0.762	−0.106	−1.0
O	0.352	0.609	−0.106	−1.0
O	0.352	0.457	−0.328	−0.8
O	−0.044	0.229	−0.328	−0.8
O	0.22	0.229	−0.328	−0.8
O(OH)	0.088	0.457	−0.106	−1.7175
H(OH)	−0.00015	0.457	−0.1434	0.7175
Si	0.352	0.305	−0.273	1.2
Si	0.088	0.152	−0.273	1.2
O	0.352	0.305	−0.106	−1.0
O	0.088	0.152	−0.106	−1.0
C(CO_2)				0.6512
O(CO_2)				−0.3256

compensating monovalent sodium ions in the interlayer region. The clay with cation exchange is discussed in Ref. [32].

Unlike *NpT* ensemble simulations used to study swelling behavior of clay minerals [17,18,37], the clay structure is fixed in our simulations. For simplicity, sheets are considered as rigid molecules; bending potential is not considered for clay sheets [38] in our work.

The potential model used for methane molecule is from the TraPPE force field [39]. For methane sorption in clay minerals, the interactions between methane and atoms of clay and with other methane molecules are described by the pairwise-additive Lennard–Jones (LJ) 12–6 potentials,

$$u_{LJ}(r_{ij}) = 4\varepsilon_{ij}\left[\left(\frac{\sigma_{ij}}{r_{ij}}\right)^{12} - \left(\frac{\sigma_{ij}}{r_{ij}}\right)^{6}\right], \quad (1)$$

where r_{ij}, ε_{ij}, and σ_{ij} are the separation, LJ well depth, and LJ size, respectively. Unlike interactions are computed using the standard Lorentz–Berthelot combining rules

$$\sigma_{ij} = \frac{\sigma_{ii} + \sigma_{jj}}{2}, \quad (2)$$

$$\varepsilon_{ij} = \sqrt{\varepsilon_{ii}\varepsilon_{jj}}. \quad (3)$$

The potential model used for CO_2 molecules is from the flexible three-site EPM2 model [40], which includes the bond-bending potential, the short-range LJ potential, and the long-range Coulomb potential. The bond-bending potential u_{bending} of each CO_2 molecule is given as [40]:

$$u_{\text{bending}}(\theta) = \frac{1}{2}k_\theta(\theta - \theta_0)^2, \quad (4)$$

where $k_\theta = 1236\,\text{kJ/mol/rad}^2$ is the bond-bending force constant, θ is the bond-bending angle between O—C—O atoms, and $\theta_0 = \pi$ rad is the equilibrium bond-bending angle. The pairwise additive Lennard–Jones and Coulomb potentials are used to compute the interactions of clay–clay, clay–CO_2, and CO_2–CO_2:

$$u(r_{ij}) = u^{LJ} + u^{C} = 4\varepsilon_{ij}\left[\left(\frac{\sigma_{ij}}{r_{ij}}\right)^{12} - \left(\frac{\sigma_{ij}}{r_{ij}}\right)^{6}\right] + \frac{q_i q_j}{4\pi\varepsilon_0 r_{ij}}, \quad (5)$$

in which q_i is the partial charge of the site. In Table 1, we also provide partial charges of CO_2 molecules. The conventional Lorentz–Berthelot combining rules are applied to obtain the LJ parameters. The LJ parameters of atoms of clay and sodium ions are based on the Dreiding [41,42] force-field. The data of the Dreiding force field do not include the parameters for the Mg atoms. We assign to Mg the same LJ parameters as in Al [43]. The charges of sodium ion and Mg atom are +1e and +2e, respectively. All the LJ parameters are listed in Table 2. The short-range LJ interactions are truncated at a distance of 1.07 nm. We place an empty space in the simulation cell along the z direction with a length much larger than L_x or L_y and use the three-dimensional *Ewald* summation with the correction term [44,45] to account for the long-range electrostatic interactions and the slab geometry.

Table 2
LJ parameters of methane, CO_2, sodium ion and atoms of clay.

Atom	ε (K)	σ (nm)
Methane		
CH_4 [39]	148.0	0.373
Carbon dioxide		
C [40]	28.129	0.2757
O [40]	80.507	0.3033
Clay		
H [41,42]	0	0
O [41,42]	78.18	0.3166
Si [41,42]	47.803	0.3951
Al [41,42]	32.707	0.4112
Mg [43]	32.707	0.4112
Sodium ion		
Na [41,42]	62.90	0.2801

2.2. Simulations

The simulations of sorption of methane and CO_2 molecules are performed in the grand canonical (μVT) ensemble. The simulation cell is placed in a rectangular box with periodicity in the x and y directions. The box size in the x direction is $L_x = 4.224$ nm, in the y direction is $L_y = 3.656$ nm. The length in the z direction is determined by the pore size of the clay and the vacuum. The pore size H is defined as the distance between the inner planes of the two sheets. The schematic representations of the clay nanopores without cation exchange and with cation exchange are shown in Figs. 2 and 3, respectively.

For simulations of methane molecules in clay nanopores, in each MC cycle, a trial random displacement is applied to all methane molecules and a methane molecule is randomly removed from or inserted into the simulation box at equal probability depending on the chemical potential of the methane reservoir outside. For simulations of CO_2 molecules in clay, in addition to the MC moves above, in every MC cycle, a trial random rotation is applied to all

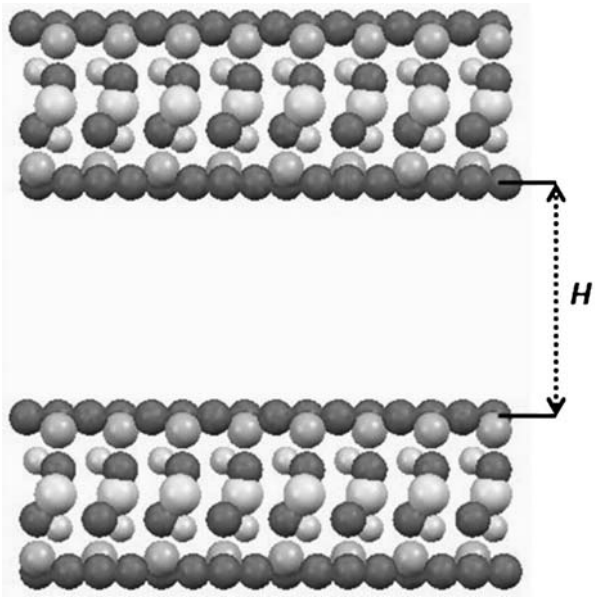

Fig. 2. The schematic representation of the structure of clay nanopore without cation exchange. The red spheres are O atoms, the white spheres are H atoms, the yellow spheres are Si atoms, and light blue spheres are Al atoms. (For interpretation of the references to color in this figure legend, the reader is referred to the web version of this article.)

CO_2 molecules. We employ a biased MC algorithm to insert and remove CO_2 molecules [15]. The vibrational degree of freedom of carbon dioxide is not incorporated in the insertion and removal of CO_2 molecules. However, we incorporate the bond bending effect in CO_2 molecule insertion/deletion. In simulations of clay with cation exchange, a trial random displacement is applied to the sodium ions in each MC cycle. The chemical potentials of methane and CO_2 molecules in the exterior reservoir are obtained from the Widom insertion method [46] in canonical (NVT) ensemble without clay minerals. The MC moves are implemented by using the Metropolis algorithm [47]. The simulation consists of 0.1 million MC cycles per absorbate molecule for equilibrium and 0.5 million MC cycles per absorbate molecule for sampling of the density profiles.

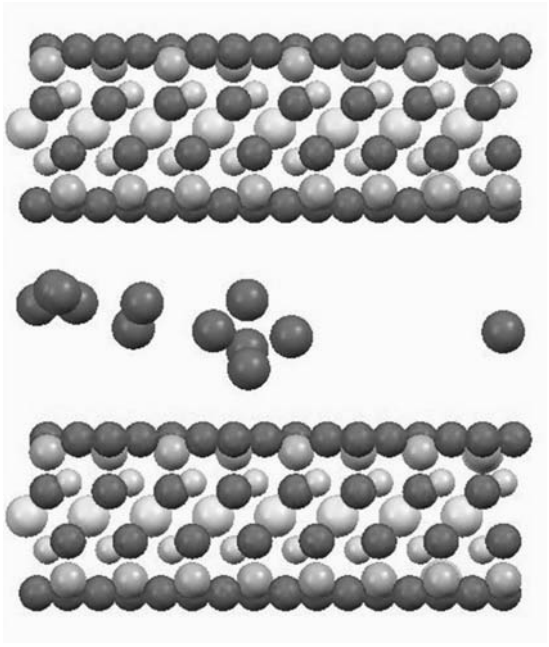

Fig. 3. The schematic representation of the structure of clay with cation exchange. The red spheres are O atoms, the white spheres are H atoms, the yellow spheres are Si atoms, light blue spheres are Al atoms, light green spheres are Mg atoms, and purple spheres are Na^+ ions. (For interpretation of the references to color in this figure legend, the reader is referred to the web version of this article.)

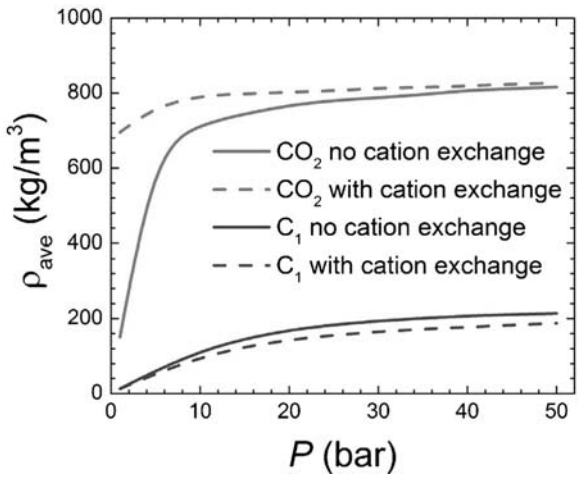

Fig. 4. The sorption isotherms of methane and CO_2 in clay nanopores with pore size $H = 1$ nm.

3. Results and discussions

We present the sorption isotherm of methane and carbon dioxide in clay nanopores and density distribution for different pore sizes and bulk densities. All of the simulations are performed at system temperature $T = 298.15$ K.

The sorption isotherms of methane and CO_2 in clay nanopores with pore size $H = 1$ nm are presented in Fig. 4. The average gas weight density ρ_{ave} in clay nanopores is given as:

$$\rho_{ave} = \frac{1}{H}\int_0^H \rho(z)dz, \tag{6}$$

where $\rho(z)$ is the weight density at distance z from one of the clay surface sheets. For CO_2 molecules, cation exchange increases gas sorption in clay nanopores, especially at low pressures. With cation exchange, CO_2 molecules are strongly sorbed in clay nanopores with a small pore size even at a low bulk pressure. For clay without cation exchange, CO_2 sorption increases significantly as pressure increases and gas sorption reaches plateau due to densely packed CO_2 molecules in the pores. The high sorption of CO_2 in clay nanopores with small pore sizes can be attributed to strong electrostatic interactions and correlations due to the two clay surfaces. On the other hand, cation exchange reduces methane sorption in clay nanopores. In contrast to CO_2 molecules, the methane–clay and methane–ion interactions are from the non-electrostatic LJ interactions. For a small pore size ($H = 1$ nm), due to the strong correlations between the two walls, the sorption of methane quickly approaches a plateau as the bulk pressure increases. The ions slightly reduce methane sorption, but the shapes of methane sorption isotherm with or without cation exchange are similar. In general, the sorption of methane is much less than that of carbon dioxide. CO_2 is a charge neutral molecule and has zero dipole moment, but it has a strong quadrupole moment [24], which increases sorption coupled with the charged clay atoms. In contrast to CO_2, methane has a zero quadrupole moment [48], thus the sorption of methane is much less than that of CO_2. Similar phenomena have also been reported

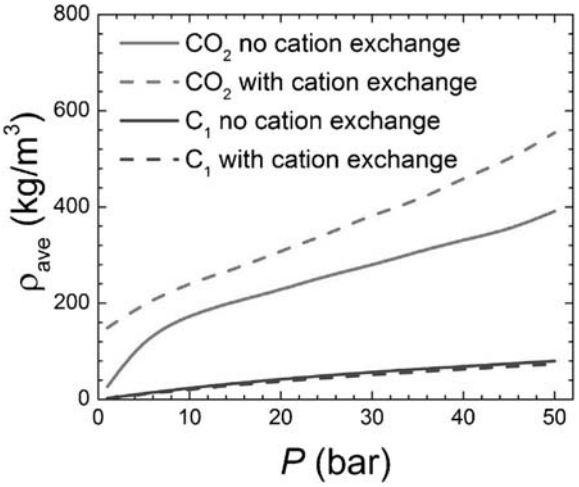

Fig. 5. The sorption isotherms of methane and CO_2 in clay nanopores with pore size $H = 4$ nm.

on gas sorption in metal-organic frameworks [49,50] and clay rock materials [12,51].

The sorption isotherms of methane and CO_2 in clay nanopores in a pore of size $H = 4$ nm are presented in Fig. 5. In contrast to pore size of $H = 1$ nm, the difference between methane and CO_2 sorption increases with the bulk pressure. This is because in large pores, the correlations between the two walls on methane sorption become weak, while the long-range electrostatic interactions affect CO_2 sorption in clay nanopores. As bulk pressure increases, methane sorption reaches a plateau indicating that methane sorption in clay nanopores is aided by surface adsorption and sorption capacity in clay minerals is closely related to surface area [6]. Similar to Fig. 4, cation exchange slightly decreases methane sorption but the two methane sorption isotherms have identical shapes. This is not the case for CO_2 sorption in clay nanopores: cation exchange enhances CO_2 sorption. Cations in the nanopores increase CO_2 sorption. Compared to the pore size of $H = 1$ nm, CO_2 sorption in a pore of size $H = 4$ nm gradually increases with bulk pressure increase. This is because the long-range electrostatic interactions between CO_2 and clay induce not only strong surface adsorption but also pore filling in the middle of pores.

We present the weight density distributions of methane and carbon dioxide molecules at bulk pressure $P = 40$ bar in clay nanopores without cation exchange with varying pore sizes in Fig. 6. While the density profiles of methane only have one peak, the density distributions of CO_2 molecules have two peaks: CO_2 molecules first adsorb on the surfaces of clay and a second layer of adsorption forms. This is probably due to the fact that the system temperature $T = 298.15$ K is higher than the critical temperature of methane (190.56 K), but slightly lower than that of CO_2 (304.14 K). In small pores ($H = 1$ nm), both CO_2 and methane molecules are highly packed due to strong correlations between the two walls. While the properties of methane molecules in the middle of the pore reach bulk limit for a pore width of $H = 2$ nm, the properties of CO_2 molecules in the middle of the pore approach the bulk only as the pore size increases. In other words, the correlation length of CO_2–clay is longer than that of methane–clay. As the pore size increases, the correlation between the two surfaces becomes weaker and the density of CO_2 molecules in the middle of the pores approach bulk limit.

In Fig. 7, we present the density distributions of methane and CO_2 molecules in clay nanopores with cation exchange at bulk pressure $P = 40$ bar. The sorption of CO_2 molecules is significantly enhanced due to the sodium ions in the clay interlayer. On the other hand, methane sorption is not significantly affected by cation exchange. Cation exchange significantly increases the CO_2/methane sorption ratio. In contrast to Fig. 6, we observe that the two peaks in CO_2 density profiles with cation exchange are both stronger than that of CO_2 without cation exchange. This is because cations further increase CO_2 sorption. In contrast to CO_2, methane-ion interactions are non-electrostatic, thus the effect of ions in

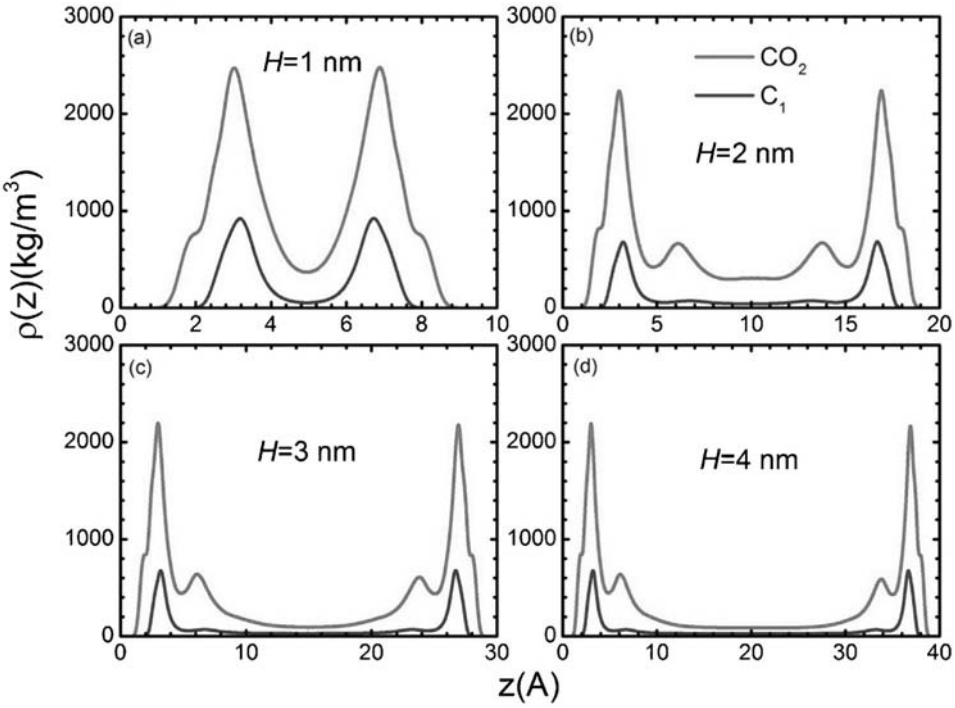

Fig. 6. The weight density distributions of methane and carbon dioxide molecules at bulk pressure $P = 40$ bar in clay nanopores without cation exchange with pore size (a) $H = 1$ nm, (b) $H = 2$ nm, (c) $H = 3$ nm, and (d) $H = 4$ nm.

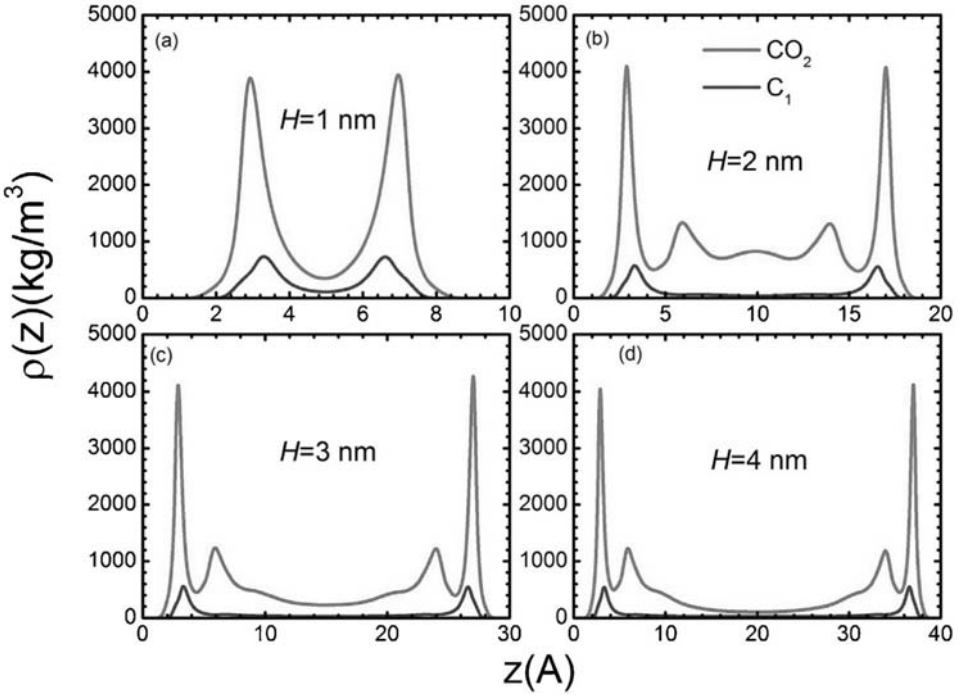

Fig. 7. The same as Fig. 6, but with cation exchange.

nanopores are negligible. Comparing Figs. 6 and 7, we observe that the increase in CO_2 sorption with cation exchange is due to stronger first and second adsorption layers than that of CO_2 without cation exchange.

The density profiles of oxygen and carbon atoms of CO_2 molecules in clay nanopores without cation exchange in different pore widths at bulk pressure $P = 40$ bar are presented in Fig. 8. In the proximity of surface, the carbon atom density profiles have only one peak. The oxygen atom density profiles have two peaks for CO_2 molecules. The distribution of carbon and oxygen atoms results in a small "bump" in the weight density profiles of CO_2 near the clay surfaces as shown in Fig. 4, which implies that the CO_2 molecules are not parallel to the surfaces. Previous studies [20–22] on CO_2 adsorption in carbon nanopores report CO_2 molecules to be parallel to the surface. The orientation of CO_2 molecules in clay nanopores is, therefore, due to the surface charge.

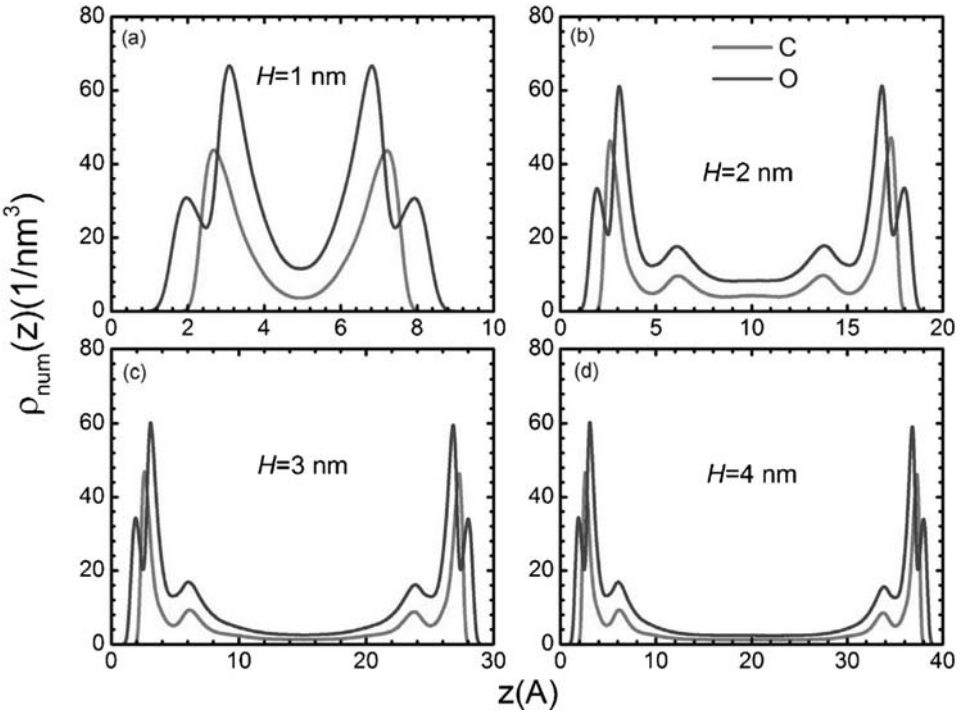

Fig. 8. The density profiles of oxygen and carbon atoms of CO_2 molecules in clay nanopores without cation exchange at bulk pressure $P = 40$ bar with pore size (a) $H = 1$ nm, (b) $H = 2$ nm, (c) $H = 3$ nm, and (d) $H = 4$ nm.

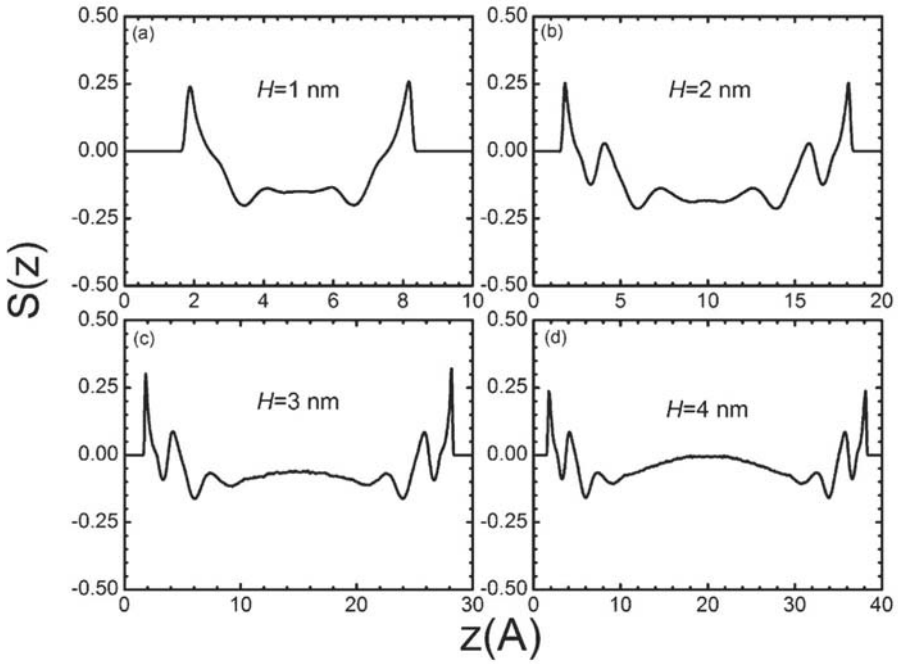

Fig. 9. The orientation order parameters of CO_2 molecules at bulk pressure $P = 40$ bar in clay nanopores without cation exchange of pore size (a) $H = 1$ nm, (b) $H = 2$ nm, (c) $H = 3$ nm, and (d) $H = 4$ nm.

The orientation of the CO_2 molecules in the pore space can be quantified using the orientation-order parameter $S(z)$ [52,53]:

$$S(z) = 1.5\langle \cos^2 \alpha \rangle - 0.5, \tag{7}$$

where α is the angle between the head-to-tail vector of the CO_2 molecule and the z axis and the bracketed term represents the ensemble average of the MC simulations. When all molecules are perpendicular to the clay surface, the orientation-order parameter is 1, if they are parallel to the surface, the value is −0.5 and when they are randomly oriented the value is 0.

Fig. 9 presents the orientation-order parameter of CO_2 molecules at bulk pressure $P = 40$ bar in various pore widths without cation exchange. In the proximity of surfaces, many of the CO_2 molecules in clay nanopores are more perpendicular to the surface. Such behavior has been reported in the study of structure of dense carbon dioxide in clay-like slit pores [19]. When a pore is small ($H \leq 3$ nm), the orientation of CO_2 molecules does not

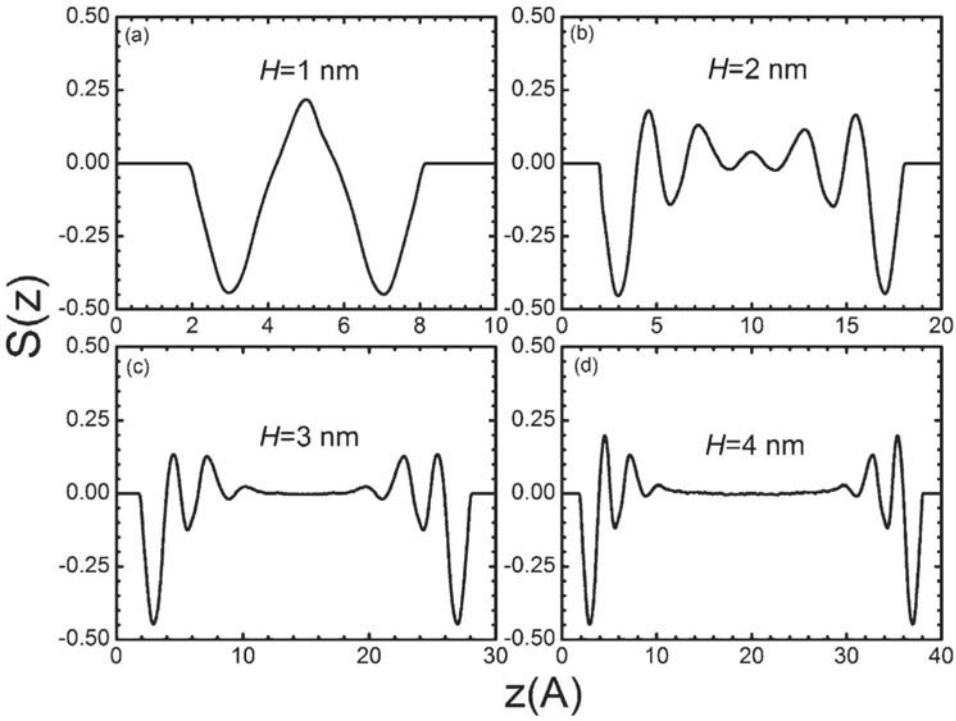

Fig. 10. The same as Fig. 9, but with cation exchange.

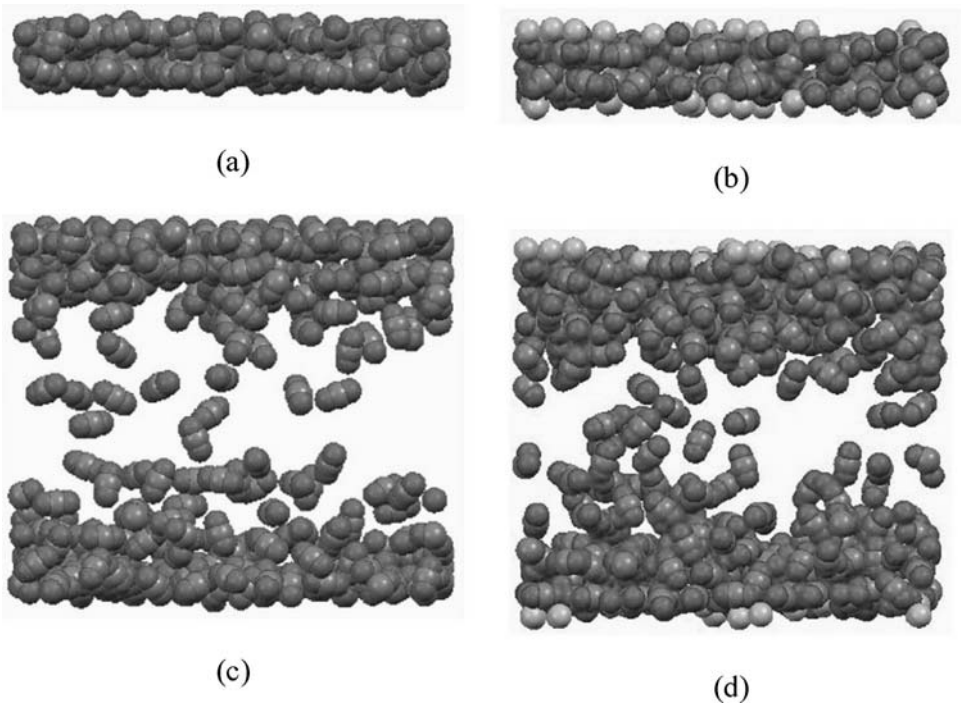

Fig. 11. The snapshot of CO_2 molecules at $P = 40$ bar in clay (a) without cation exchange, $H = 1$ nm, (b) with cation exchange, $H = 1$ nm, (c) without cation exchange, $H = 4$ nm, (d) with cation exchange, $H = 4$ nm. The gray spheres are C, the red spheres are O, and light blue spheres are Na. The structure of clay is omitted. (For interpretation of the references to color in this figure legend, the reader is referred to the web version of this article.)

reach bulk limit because of strong long-range electrostatic interactions from the two walls. For large pores ($H = 4$ nm), the orientation of CO_2 molecules becomes the bulk limit in the middle of the pores, because the correlation between charges of the two surfaces becomes weaker.

We present the orientation-order parameter of CO_2 molecules with cation exchange at bulk pressure $P = 40$ bar in various pore sizes in Fig. 10. In contrast to Fig. 9, the orientation of CO_2 molecules is more parallel in proximity of surfaces. This is because the sodium ions are attracted to the surface and the presence of sodium ions eases CO_2 molecules to lay parallel to the surface. For pore size $H \geq 3$ nm, the properties of CO_2 molecules in the middle of the pore approach the bulk limit.

To have a better understanding of the structure of CO_2 molecule in various pores, we present snapshots of CO_2 molecules in Fig. 11. In a small pore ($H = 1$ nm), CO_2 molecules are mainly attracted to the

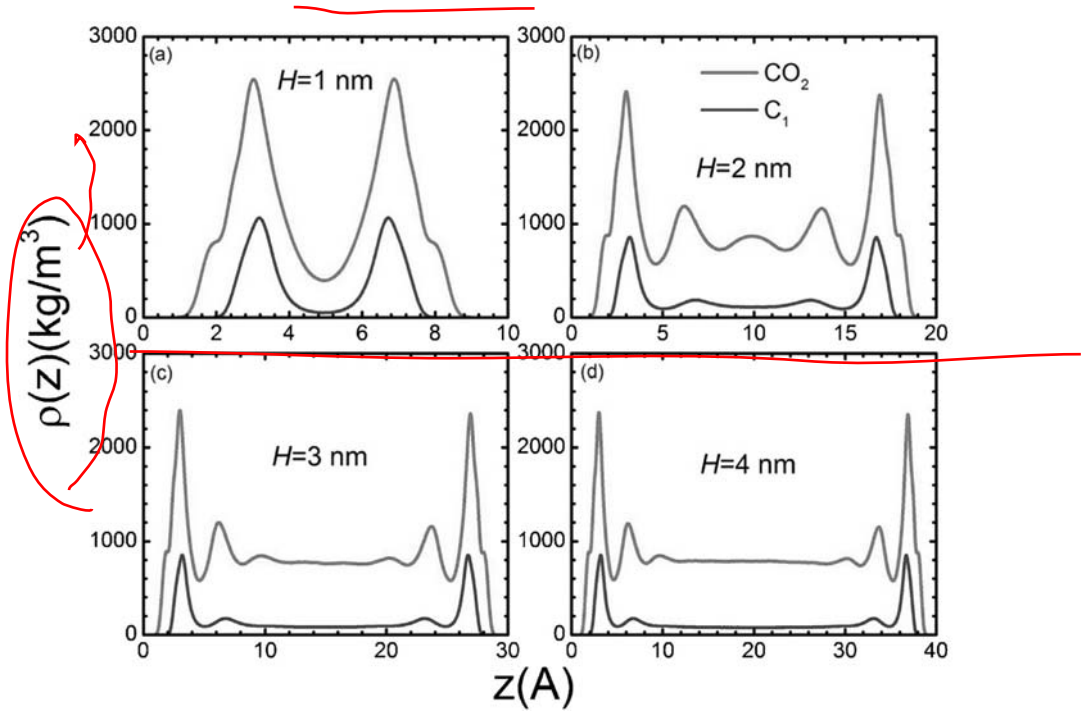

Fig. 12. The same as Fig. 6, but at bulk pressure $P = 100$ bar.

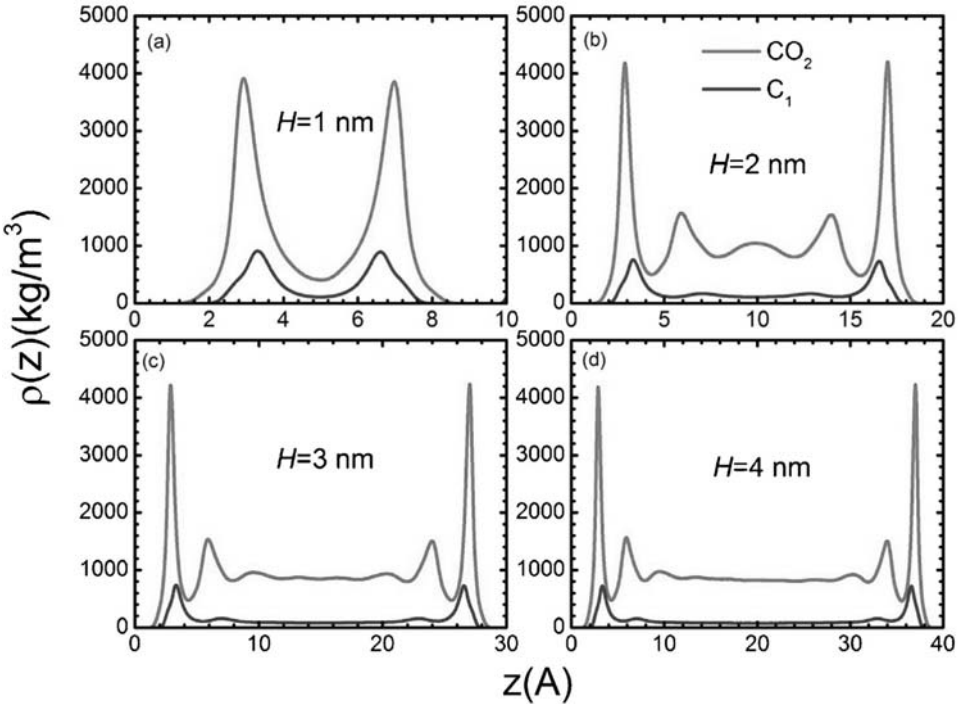

Fig. 13. The same as Fig. 7, but at bulk pressure $P = 100$ bar.

clay surface in the proximity of the surface. The orientations of CO_2 molecules with cation exchange are closer to parallel at the surface, while CO_2 molecules in a clay without cation exchange is closer to perpendicular at the surface. For a larger pore ($H = 4$ nm), the orientation of CO_2 molecules remains the same as in the small pore near the surface. However, in contrast to CO_2 molecules without cation exchange, we observe a stronger second layer with cation exchange. In both the 1 and 4 nm pore sizes, sodium ions are mainly attracted to the clay due to the negatively charged clay sheets.

The weight density distributions of methane and carbon dioxide molecules at bulk pressure $P = 100$ bar in clay nanopores without cation exchange in different pore sizes are presented in Fig. 12. At this pressure, methane is in the supercritical region and CO_2 is in the bulk liquid state. The density of CO_2 in the middle of the pores is about the same at $H = 3$ and 4 nm. There is a weak second methane adsorption layer; the second layer of CO_2 molecules becomes more pronounced. The first layer of CO_2 adsorption is affected by the clay charge and CO_2–clay dispersive interactions. The second layer of adsorption is due to clustering of CO_2 molecules. In contrast to Fig. 6, with the bulk pressure increase in Fig. 12, the first adsorption layer of CO_2 density profiles becomes somewhat stronger, but the major contribution to CO_2 sorption in larger pores ($H \geq 2$ nm) at higher pressure is from the pore filling in the middle of the pores. On the other hand, as the pressure increases, there is an increase in adsorption layer of methane density profiles. The weight density distributions of methane and carbon dioxide molecules at bulk pressure $P = 100$ bar in clay nanopores with cation exchange at different pore sizes are presented in Fig. 13. In contrast to Fig. 12, with cation exchange, stronger first and second adsorption layer of CO_2 density profiles are observed, while in large pores ($H \geq 3$ nm) CO_2 densities approach bulk limit in the middle of the pores. This is an indication that CO_2 molecules can accumulate around cations to further increases CO_2 sorption. However, at high pressure, the adsorption layer of CO_2 screens the charges of cations and the effect of cations on CO_2 molecule accumulation in the middle of the pores is negligible. Therefore, pore filling in the middle of the pores is aided by the first and second adsorption layer of CO_2. Similar to Fig. 7, the effect of cation exchange on methane density distributions is insignificant.

4. Conclusions

Our investigation reveals that methane adsorption in clay mineral is dominated by the dispersive clay–methane interactions and as the pore size increases, the sorption mainly occurs in the proximity of the clay surface. This is because the dispersive interactions are relatively short-ranged. The system temperature selected is higher than the critical temperature of methane; as a result the density profile of methane in clay has only one peak near the surface and a weak second peak forms only at high bulk reservoir pressures. Our work implies that the sorption of methane in clay nanopores is mainly dominated by the surface area of the pores, since a second adsorption layer does not form in methane sorption. This result is in line with recent experiments [6].

The charge of clay is the main contribution to the sorption of CO_2 molecules. The cation exchange of clay minerals further increases sorption of CO_2 molecules. The clay charge results in a large difference in methane and CO_2 sorption in clay minerals in line with experiments [12,51]. The clay charge contributes to the non-parallel orientation behavior of CO_2 molecules near the clay surfaces. With cation exchange, the first layer of adsorption is easily filled by CO_2 molecules and CO_2 molecules become parallel to the clay surface near the wall. In general, the sorption of CO_2 in clay starts with the formation of the first layer of adsorption near the clay surface and as the bulk pressure increases, then a less prominent second layer of adsorption forms. At low pressure, CO_2 sorption is dominated by surface and cation charges which form a strong adsorption layer. As pressure increases, CO_2 sorption is further enhanced by the pore filling in the middle of the pores.

The main conclusion from this work is that the clay atom charges and cation exchange affect sorption and orientation of CO_2 molecules in clay minerals, while methane sorption is dominated by dispersive clay–methane interactions and sorption is related to the surface area of the clay minerals. As an important component

of shale rocks, gas sorption in clays may not be neglected. Our simulation results provide a fundamental understanding toward the estimation of gas-in-place study in the clay media of the shale. We plan to expand the work on clay to include the effect of water on sorption of carbon dioxide and methane. The picture will be completed when we expand our research into phase behavior to include organic materials in shale.

Acknowledgement

This work was supported by member companies of the Reservoir Engineering Research Institute. Their support is greatly appreciated.

References

[1] M. Gasparik, A. Ghanizadeh, P. Bertier, Y. Gensterblum, S. Bouw, B.M. Krooss, Energy & Fuels 26 (2012) 4995–5004.
[2] S.L. Montgomery, D.M. Jarvie, K.A. Bowker, R.M. Pollastro, AAPG Bulletin 89 (2005) 155–175.
[3] D.J.K. Ross, R. Marc Bustin, Marine and Petroleum Geology 26 (2009) 916–927.
[4] D.J.K. Ross, R.M. Bustin, AAPG Bulletin 92 (2008) 87–125.
[5] P. Weniger, W. Kalkreuth, A. Busch, B.M. Krooss, International Journal of Coal Geology 84 (2010) 190–205.
[6] L. Ji, T. Zhang, K.L. Milliken, J. Qu, X. Zhang, Applied Geochemistry 27 (2012) 2533–2545.
[7] R. Aringhieri, Clays and Clay Minerals 52 (2004) 700–704.
[8] C.-C. Wang, L.-C. Juang, C.-K. Lee, T.-C. Hsu, J.-F. Lee, H.-P. Chao, Journal of Colloid and Interface Science 280 (2004) 27–35.
[9] P.D. Schettler Jr., C.R. Parmely, J.C., SPE J, SPE 23422, 1991.
[10] X.-C. Lu, F.-C. Li, A.T. Watson, SPE Formation Evaluation, SPE 26632, 1995.
[11] A. Busch, S. Alles, Y. Gensterblum, D. Prinz, D.N. Dewhurst, M.D. Raven, H. Stanjek, B.M. Krooss, International Journal of Greenhouse Gas Control 2 (2008) 297–308.
[12] C. Volzone, J.G. Thompson, A. Melnitchenko, J. Ortiga, S.R. Palethorpe, Clays and Clay Minerals 47 (1999) 647–657.
[13] A.-L. Cheng, W.-L. Huang, Organic Geochemistry 35 (2004) 413–423.
[14] Y. Liu, J. Wilcox, International Journal of Coal Geology 104 (2012) 83–95.
[15] E.J.M. Hensen, T.J. Tambach, A. Bliek, B. Smit, The Journal of Chemical Physics 115 (2001) 3322–3329.
[16] D.E. Smith, Langmuir 14 (1998) 5959–5967.
[17] D.A. Young, D.E. Smith, The Journal of Physical Chemistry B 104 (2000) 9163–9170.
[18] N.T. Skipper, K. Refson, J.D.C. McConnell, The Journal of Chemical Physics 94 (1991) 7434–7445.
[19] X. Yang, C. Zhang, Chemical Physics Letters 407 (2005) 427–432.
[20] S.K. Bhatia, K. Tran, T.X. Nguyen, D. Nicholson, Langmuir 20 (2004) 9612–9620.
[21] S. Samios, A.K. Stubos, N.K. Kanellopoulos, R.F. Cracknell, G.K. Papadopoulos, D. Nicholson, Langmuir 13 (1997) 2795–2802.
[22] A. Vishnyakov, P.I. Ravikovitch, A.V. Neimark, Langmuir 15 (1999) 8736–8742.
[23] M. Heuchel, G.M. Davies, E. Buss, N.A. Seaton, Langmuir 15 (1999) 8695–8705.
[24] F. Sylwester, P.T. Artur, A.G. Piotr, J.F.H. Peter, K. Piotr, Journal of Physics: Condensed Matter 21 (2009) 315005.
[25] Y. Liu, J. Wilcox, Environmental Science & Technology 47 (2012) 95–101.
[26] C.M. Tenney, C.M. Lastoskie, Environmental Progress 25 (2006) 343–354.
[27] P. Giesting, S. Guggenheim, A.F. Koster van Groos, A. Busch, International Journal of Greenhouse Gas Control 8 (2012) 73–81.
[28] L. Wang, M. Zhang, S.A.T. Redfern, Clays and Clay Minerals 51 (2003) 439–444.
[29] R.T. Cygan, V.N. Romanov, E.M. Myshakin, The Journal of Physical Chemistry C 116 (2012) 13079–13091.
[30] V. Marry, P. Turq, T. Cartailler, D. Levesque, The Journal of Chemical Physics 117 (2002) 3454–3463.
[31] G. Sposito, N.T. Skipper, R. Sutton, S.-h. Park, A.K. Soper, J.A. Greathouse, Proceedings of the National Academy of Sciences 96 (1999) 3358–3364.
[32] M. Chavez-Paez, K.V. Workum, L.d. Pablo, J.J.d. Pablo, The Journal of Chemical Physics 114 (2001) 1405–1413.
[33] N.T. Skipper, F.-R. Chou Chang, G. Sposito, Clays and Clay Minerals 43 (1995) 285–293.
[34] L. de Pablo, M.L. Chávez, J.J. de Pablo, Langmuir 21 (2005) 10874–10884.
[35] F.-R.C. Chang, N.T. Skipper, G. Sposito, Langmuir 11 (1995) 2734–2741.
[36] F.-R.C. Chang, N.T. Skipper, G. Sposito, Langmuir 13 (1997) 2074–2082.
[37] N.T. Skipper, G. Sposito, F.-R. Chou Chang, Clays and Clay Minerals 43 (1995) 294–303.
[38] R.T. Cygan, J.-J. Liang, A.G. Kalinichev, The Journal of Physical Chemistry B 108 (2004) 1255–1266.
[39] M.G. Martin, J.I. Siepmann, The Journal of Physical Chemistry B 102 (1998) 2569–2577.
[40] J.G. Harris, K.H. Yung, The Journal of Physical Chemistry 99 (1995) 12021–12024.
[41] K.S. Smirnov, D. Bougeard, The Journal of Physical Chemistry B 103 (1999) 5266–5273.
[42] S.L. Mayo, B.D. Olafson, W.A. Goddard, The Journal of Physical Chemistry 94 (1990) 8897–8909.
[43] Q.H. Zeng, A.B. Yu, G.Q. Lu, R.K. Standish, Chemistry of Materials 15 (2003) 4732–4738.
[44] I.-C. Yeh, M.L. Berkowitz, The Journal of Chemical Physics 111 (1999) 3155–3162.
[45] P.S. Crozier, R.L. Rowley, E. Spohr, D. Henderson, The Journal of Chemical Physics 112 (2000) 9253–9257.
[46] B. Widom, The Journal of Chemical Physics 39 (1963) 2808–2812.
[47] N. Metropolis, A.W. Rosenbluth, M.N. Rosenbluth, A.H. Teller, E. Teller, The Journal of Chemical Physics 21 (1953) 1087–1092.
[48] P. Rallapalli, K. Prasanth, D. Patil, R. Somani, R. Jasra, H. Bajaj, Journal of Porous Materials 18 (2011) 205–210.
[49] Y.-S. Bae, O.K. Farha, J.T. Hupp, R.Q. Snurr, Journal of Materials Chemistry 19 (2009) 2131–2134.
[50] P. Chowdhury, S. Mekala, F. Dreisbach, S. Gumma, Microporous and Mesoporous Materials 152 (2012) 246–252.
[51] A. Melnitchenko, J.G. Thompson, C. Volzone, J. Ortiga, Applied Clay Science 17 (2000) 35–53.
[52] S.K. Singh, A. Sinha, G. Deo, J.K. Singh, The Journal of Physical Chemistry C 113 (2009) 7170–7180.
[53] I. Bitsanis, G. Hadziioannou, The Journal of Chemical Physics 92 (1990) 3827–3847.